

# Enhanced Electrolyte Transport and Kinetics Mitigate Graphite Exfoliation and Li Plating in Fast-Charging Li-Ion Batteries

Hongpeng Gao, Qizhang Yan, John Holoubek,\* Yijie Yin, Wurigumula Bao, Haodong Liu, Artem Baskin, Mingqian Li, Guorui Cai, Weikang Li, Duc Tran, Ping Liu, Jian Luo, Ying Shirley Meng, and Zheng Chen\*

Despite significant progress in energy retention, lithium-ion batteries (LIBs) face untenable reductions in cycle life under extreme fast-charging (XFC) conditions, which primarily originate from a variety of kinetic limitations between the graphite anode and the electrolyte. Through quantitative Li<sup>+</sup> loss accounting and comprehensive materials analyses, it is directly observed that the operation of LIB pouch cells at 4 C||C/3 (charging||discharging) results in Li plating, disadvantageous solid-electrolyte-interphase formation, and solvent co-intercalation leading to interstitial decomposition within graphite layers. It is found that these failure modes originate from the insufficient properties of conventional electrolytes, where employing a designed ester-based electrolyte improved the capacity retention of these cells from 55.9% to 88.2% after 500 cycles when operated at the aforementioned conditions. These metrics are the result of effective mitigation of the aforementioned failure modes due to superior Li<sup>+</sup> transport and desolvation characteristics demonstrated through both experimental and computational characterization. This work reveals the vital nature of electrolyte design to XFC performance.

## 1. Introduction

The widespread adoption of lithium-ion battery (LIB) powered electric vehicles (EVs) is a vital step in the transition to a future based on sustainable energy sources.<sup>[1]</sup> Though substantial progress has been made in extending the driving range of EVs due to advancements in LIB energy density, battery charging times lag far behind standard refueling periods for gas-powered automobiles. To address this, the US Department of Energy has set an ambitious extreme fast-charge (XFC) goal to achieve charging times of 15 min or less without a significant reduction in energy density or cycle life of the cell.<sup>[2]</sup> To achieve and exceed this benchmark, various limiting kinetic processes within high-energy LIBs must be optimized and understood. In principle, the kinetic limitations of LIB operation are considered to be diffusion

of Li<sup>+</sup> within the bulk of the electrode materials, migration of Li<sup>+</sup> through the solid-electrolyte-interphase (SEI), diffusion of Li<sup>+</sup> through the electrolyte bulk, and charge-transfer at the electrode interphase.<sup>[3,4]</sup>

Though there is a deep history in the literature on improving the performance retention of battery electrode materials at a high rate of 4 C or above, achieving adequate energy density and cycle stability in concert with the aforementioned charging times remains an immense challenge. Though alternative electrode materials designed for high-rate cycling exist, none have projected energy densities comparable to graphite anodes and transition-metal oxide cathodes.<sup>[5,6]</sup> However, maintaining the electrode materials and loadings required for EV – level energy density results in extreme cyclability and safety tradeoffs for high-rate cycling. Cathode materials have been shown to face reduced capacity retention at high rates due to insufficient kinetics associated with micron-scale particles, placing undue strain on the electrode composite.<sup>[2]</sup> In this regard, previous works have found that elevated charging rates increase cathode particle strain, exacerbate surface reorganization, and leads to the formation of more resistive interphases, all of which impact long-term fast-charge cyclability.<sup>[7,8]</sup> However, evidence also exists that a significant portion of these losses in the NMC


H. Gao, Q. Yan, Y. Yin, M. Li, G. Cai, P. Liu, J. Luo, Y. S. Meng, Z. Chen  
Program of Materials Science  
University of California San Diego  
9500 Gilman Drive, La Jolla, California 92093, USA  
E-mail: zhengchen@eng.ucsd.edu

H. Gao, Q. Yan, J. Holoubek, Y. Yin, W. Bao, H. Liu, M. Li, G. Cai, W. Li,  
P. Liu, J. Luo, Y. S. Meng, Z. Chen  
Department of NanoEngineering  
University of California San Diego  
9500 Gilman Drive, La Jolla, California 92093, USA  
E-mail: jholoubek@eng.ucsd.edu

A. Baskin  
NASA Ames Research Center  
Moffett Field, CA 94035, USA

W. Li, D. Tran, P. Liu, Y. S. Meng, Z. Chen  
Program of Chemical Engineering  
University of California San Diego  
9500 Gilman Drive, La Jolla, California 92093, USA

P. Liu, J. Luo, Y. S. Meng, Z. Chen  
Sustainable Power & Energy Center (SPEC)  
University of California San Diego  
9500 Gilman Drive, La Jolla, California 92093, USA

 The ORCID identification number(s) for the author(s) of this article can be found under <https://doi.org/10.1002/aenm.202202906>.

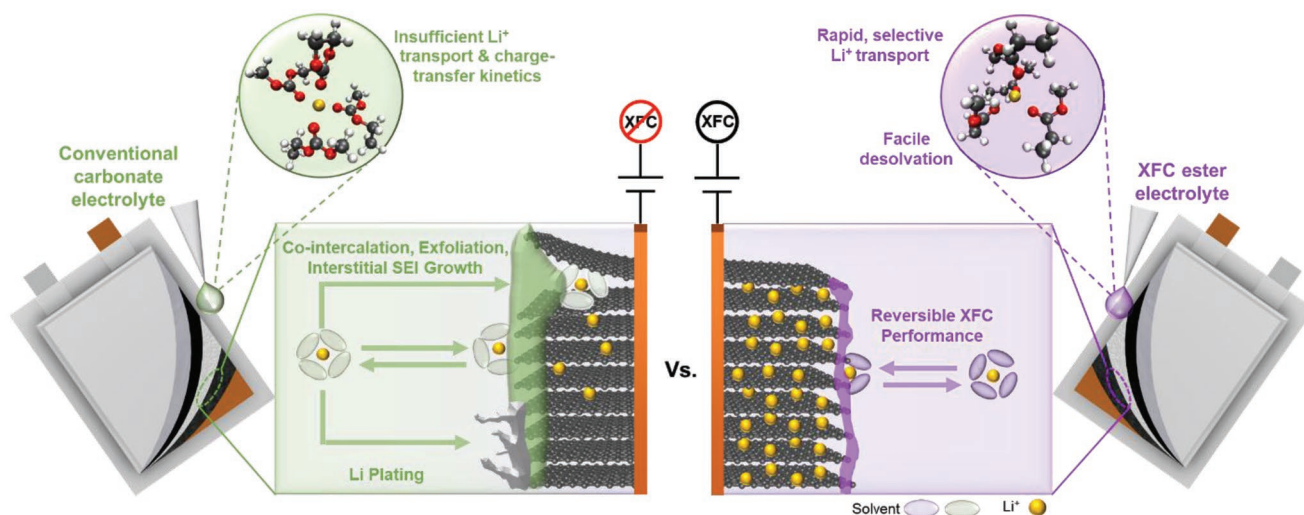
DOI: 10.1002/aenm.202202906

cathodes can be recovered in the presence of renewed  $\text{Li}^+$  inventory.<sup>[9]</sup> Additionally, a number of acute limitations for the retention of energy and cycle are associated with the graphite anode.<sup>[10–12]</sup> Specifically, the proximity of the  $\text{LiC}_6$  redox potential to  $\text{Li}/\text{Li}^+$  has been shown to lead to  $\text{Li}$  metal plating, which leads to rapid cell failure, and causes immense safety concerns due to internal shorting from dendritic growth.<sup>[8,11,12]</sup> To mitigate these issues, researchers have demonstrated a variety of electrode design methods, including patterning of graphite anode architectures<sup>[13–15]</sup> and increasing the active surface area either by modification of the graphite itself or the inclusion of high-area carbons within the composite.<sup>[16,17]</sup> Though they may be a promising route forward in some form, these strategies generally result in greater void space within the electrodes, increasing the minimum allowable electrolyte loading, giving rise to the reduced total energy density at scale.<sup>[18,19]</sup> Though the rational design of the charging protocol is also a vital direction, rapid storage kinetics is still necessary.<sup>[20]</sup> In this regard, a number of strategies exist for electrode optimization, but many phenomena at the electrode/electrolyte interphase remains to be fully discovered and addressed.

Design of the battery electrolyte has been demonstrated to have a transformational effect on the performance retention of LIBs under XFC conditions. Generally, improving the bulk ionic conductivity and transference number has been considered as a crucial strategy, where Colclasure et al. has demonstrated a correlation between  $\text{Li}^+$  depletion at the interphase to the induction of  $\text{Li}$  plating.<sup>[21,22]</sup> These effects are therefore exacerbated in practical cells with increased electrode loadings and non-negligible effects from alignment and porosity.<sup>[22,23]</sup> Additionally, the inclusion of additives known to form low-impedance SEI components have been a focus of development.<sup>[24–26]</sup> In this regard, electrolyte composed of low-viscosity solvents which offer rapid  $\text{Li}^+$  diffusion, e.g. methyl acetate (MA) have shown great promise for energy density retention at high rates.<sup>[26–31]</sup> Moreover, work from Du et al. has demonstrated that variations in salt chemistry may also produce such improvements.<sup>[29]</sup> However, the electrochemical stability of these unorthodox solvents tends to yield reduced cycle life compared to conventional

carbonate systems, and raise concerns associated with gas generation during cycling.<sup>[27]</sup> In addition to the SEI and bulk transport, recent evidence suggests that the solvation structure of  $\text{Li}^+$  within the electrolyte dictates the desolvation-related charge-transfer impedance at the interphase.<sup>[32–36]</sup> In this regard, electrolytes which improve performance at reduced temperatures, where  $\text{Li}^+$  desolvation dictates overall kinetics, may prove to be a valuable design metric. Hence, discovery of a battery electrolyte with rapid  $\text{Li}^+$  transport, facile charge transfer, low-impedance interphases, and exceptional electrochemical stability is vital to enable 4 C or above charging and understanding the processes of interest at the electrolyte/electrode interphase under kinetic strain.

Herein, we present an analysis of the rate-induced anode failure of  $\text{LiNi}_{0.6}\text{Mn}_{0.2}\text{Co}_{0.2}$  (NMC 622) || graphite full pouch cells employing conventional carbonate electrolytes when run under XFC conditions. We demonstrate clear evidence that the graphite anode in cells employing conventional electrolytes undergoes severe capacity decay due to loss of  $\text{Li}$  through  $\text{Li}$  plating, dislocation of isolated graphite, and exfoliation-driven interstitial SEI formation due to insufficient charge-transfer kinetics. Further, we comprehensively address each of these failures with proper selection, design, and application of a carboxylate ester-based electrolyte. This optimized electrolyte, 1 M lithium hexafluorophosphate ( $\text{LiPF}_6$ ) methyl propionate (MP) + 10% fluoroethylene carbonate (FEC) (M9F1) enabled the retention of 82.5% cell energy density when charged at 4 C (15 min) compared to only 73.4% for cells employing the conventional 1.2 M  $\text{LiPF}_6$  in 3:7 ethylene carbonate (EC)/ethyl methyl carbonate (EMC) (Gen 2) blend. Moreover, cells employing M9F1 were found to demonstrate 88.2% and 77.9% capacity retention after 500 and 1000 cycles, respectively, compared to only 54.1% and 12.4% in Gen 2. The ability of M9F1 to circumvent the aforementioned failure conditions was found to be a result of improved ionic conductivity, high transference number, a favorable solvation structure allowing facile charge transfer, and the formation of a thin SEI of favorable composition (Scheme 1). This work unambiguously presents the compounding failure modes of LIBs under XFC protocols while



**Scheme 1.** Impact of electrolyte chemistry on the typical failure modes of XFC lithium-ion batteries.

demonstrating the transformational effect of electrolyte composition on such processes and the resulting performance.

## 2. Experimental Section

### 2.1. Materials and Experimental Methods

#### 2.1.1. Materials

LP40 (1.0 M LiPF<sub>6</sub> in EC/DMC = 50/50 (v/v)), methyl propionate (MP, 99%), methyl acetate (MA, anhydrous 99.5%) and methyl butyrate (MB, 99%) were purchased from Sigma. Gen 2 (1.2 M LiPF<sub>6</sub> in EC/EMC 3:7 w/w) and lithium hexafluorophosphate (LiPF<sub>6</sub>) were purchased from Gotion and used as received. The Fluoroethylene carbonate (FEC, 98.0%) was purchased from TCI America. MP, MA MB, and FEC were soaked in molecular sieve (10 Angstrom, Sigma) overnight before use.

#### 2.1.2. Coin Cell Preparation

The cathode composition is LiNi<sub>0.6</sub>Co<sub>0.2</sub>Mn<sub>0.2</sub>O<sub>2</sub> (Canrd Ltd.)/PVDF (Kynar HSV 1800)/carbon black (Super-P) at 90:5:5 wt.% ratio. The areal capacity is 2.7 mAh cm<sup>-2</sup>. The anode composition is graphite (Carnad Ltd.)/ (Kynar HSV 1800)/carbon black (Super-P) at 90:5:5 wt.% ratio. The anode areal capacity is 3 mAh cm<sup>-2</sup>. The slurries of cathode and anode materials was casted on aluminum and copper foils, respectively. Both cathode and anode electrodes were transferred into vacuum oven for drying overnight at 120 °C and 80 °C, respectively. CR-2032 type coin cells were assembled with prepared cathodes and anodes (N/P ratio = 1.1) with a trilayer membrane (Celgard 2325) as the separator soaked with 80 μL of electrolyte.

#### 2.1.3. Electrochemical Testing

All electrochemical data provided in this work were produced by CR2032 coin cells and heat-sealed multilayer pouch cells assembled in an Ar-filled glovebox kept at <0.5 ppm O<sub>2</sub> and <0.1 ppm H<sub>2</sub>O. The NCM622||graphite dry pouch cells (Figure S21, Supporting Information) were made by Carnad Ltd. The dry pouch cells (Carnad Ltd) were filled with 1 mL of electrolyte (4.7 g Ah<sup>-1</sup>) and sealed by vacuum sealer machine (MTI Corp.). The low-temperature data points were obtained from these cells inside a SolidCold C4-76A chamber for -40 °C testing. All potentiostatic tests were carried out on a Biologic VSP-300 potentiostat.

The NC622||graphite cells (CR-2032 type) were utilized for investigating the optimized MP/FEC ratio for fast charging purposes. The coin cells were galvanostatically activated from 2.8 V to 4.3 V at 0.1C (1C = 180 mAh g<sup>-1</sup>) for 5 cycles before testing. The coulombic efficiency and specific capacity were analyzed at the first cycles of 4C/0.1C mode. Battery cyclers (Neware BTS-4000) were used for electrochemical cycling.

Pouch cells were galvanostatically activated from 2.8 V to 4.3 V at 23 mA (0.1C) for 5 cycles before testing. Both constant

current (CC) with a charging voltage cutoff of 4.3 V and constant current- constant voltage (CC-CV) charging protocol with a charging time cutoff (15 min for 4C and 10 min for 6C) were operated for testing the capacity retention in designed electrolytes. For 15 min/10 min fast charging, the activated pouch cells were charged at a CC mode until reaching an upper voltage cutoff 4.3 V and then held the potential until the total time (CC+CV) reached 15 min/10 min. The discharging rate was set at C/3 with a voltage cutoff of 2.7 V. The galvanostatic testing was done on an Arbin LBT-10V5A system.

For the low-temperature rate-capability test, the pouch cells were galvanostatically charged to 4.3 V under room temperature and then discharged to 2.8 V at different rates after switching the temperature to -40 °C. Cells are soaking for at least 2 h to reach the target temperature. The galvanostatic testing of pouch cells was done on an Arbin LBT-10V5A system. EIS tests of NC622||graphite pouch cells were performed on a Biologic VSP-300 potentiostat with a 10 mV perturbation in the frequency range of 1 MHz to 100 mHz.

The transference numbers of all the electrolytes were measured by a potentiostatic polarization technique on a Biologic VSP-300 potentiostat. A Li||Li CR2032 coin cell with five Celgard 2325 separators filled by a designed electrolyte was applied 5 mV for 2 h to obtain the initial current  $I_0$ . When the cation concentration is uniform and the current corresponds to both the cations and anions, the steady state current  $I_{ss}$ , is only attributed to the cations. The cell impedance before and after the polarization was obtained EIS spectra. Thus, the transference number was then calculated using the following equation:

$$t_+ = \frac{I_{ss}(\Delta V - I_0 R_0)}{I_0(\Delta V - I_{ss} R_{ss})} \quad (1)$$

#### 2.1.4. Electrolyte Thermal Stability Measurements

The thermogravimetric analysis (TGA) and differential scanning calorimetry (DSC) curve of electrolytes were tested in sealed aluminum pans by a SDT 650 simultaneous DSC/TGA in UC San Diego Materials Research Science and Engineering Center (UCSD MRSEC).

#### 2.1.5. Electrolytic Conductivity Measurements

The ionic conductivity of the electrolytes was measured by customized stainless-steel two-electrode cells. Two polished stainless-steel (SS 316L) were spaced symmetrically as electrodes. The cell constant was calibrated from 0.447 to 80 mS cm<sup>-1</sup> by using OAKTON standard conductivity solution. The data for ionic conductivities were measured by LabView Software. An ESPEC BTX-475 temperature chamber was utilized for testing data points at a temperature from 60 to -60 °C. To maintain the cell at a set temperature, a 45 min interval was applied during measurement. The ionic conductivities were calculated using the following equation:  $\sigma_i = L/(A \times R)$ , where  $L$  and  $A$  are the length and area of internal space between the electrodes, respectively, and  $R$  is the solution resistance.

$$\sigma = \frac{L}{A \times R} \quad (2)$$

### 2.1.6. Cell Gassing Test

Cell gassing tests were performed with NCM622||Gr pouch cells (cell capacity  $\approx 250$  mAh). The evolution of gas volume during XFC cycling was measured via the Arrhenius method according to Dahn et al.<sup>[37]</sup> As shown in Figure S21, Supporting Information, cells were weighed while submerged in deionized water (18 M $\Omega$  cm) before and after the experiment. The volume of generated gas is directly proportional to the difference in weight of the pouch cell while submerged in water. The volume of the gas generated after cycling was calculated by the following equation:

$$\text{Volume of gas generation} = \left( \frac{\text{Weight of the cell in water before cycling} - \text{Weight of the cell in water after cycling}}{\text{Density of water}} \right) \quad (3)$$

### 2.1.7. Materials Characterization

The electrode cross-section experiments were performed using a FEI Scios DualBeam FIB/SEM. Cryo stage was used to prevent ion beam damage on the Li metal on the graphite electrodes. During ion beam milling, the cryo-stage temperature was maintained at  $\approx -180$  °C. Cryo-TEM study was conducted using a JEOL 2800 TEM at 200 kV.

AC-STEM and EDX experiment was conducted using a JEOL JEM-ARM 300F at 300 kV. To prevent electron beam damage on the SEI, Gatan 626 cooling holder was used to maintain the sample temperature at  $\approx -170$  °C during the TEM session. To fabricate the lamella samples, a dual-beam focused ion beam FIB/SEM FEI Scios was used to lift out the lamella from the cycled electrodes. Sample transfer in/out of the FIB/SEM was performed using an air-free quick-loader (FEI) under a vacuum. The sample transfer in/out of the TEM was performed using an Ar-purged glove bag. The sample preparation and transfer were performed with minimum contact with ambient air. The detailed procedure was illustrated in Figure S19, Supporting Information.

XPS was performed using an AXIS Supra XPS from Kratos Analytical using a monochromatized Al K $\alpha$  radiation under  $10^{-9}$  Torr chamber pressure. The sample transfer was performed using the nitrogen-filled glovebox directly attached to the XPS. For the depth profile experiment, a 5 keV Ar1000+ ion cluster was used to etch the electrode for 30 s. All spectra were analyzed using CasaXPS software.

Raman (Renishaw inVia/Bruker Innova) was performed with 532 nm illumination, provided by a Modu-Laser 50 mW Ar+ ion laser. The samples were prepared by placing the electrode onto a coverslip and sealed with Kapton tape in glovebox.

All X-ray diffraction (XRD) samples were prepared by placing the electrode onto a coverslip and sealed with Kapton tape in the glovebox. Their crystal structures were examined by X-ray

powder diffraction (XRD) employing a Rigaku Miniflex (Cu K $\alpha$  radiation,  $\lambda = 1.5406$  Å) from a scanning rate of 2 deg min $^{-1}$ .

### 2.1.8. Neutron Diffraction mapping

The time-of-flight (TOF) powder neutron diffraction data were collected on VULCAN beamline at the Spallation Neutron Sources (SNS) of Oak Ridge National Lab (ORNL). The pouch cell was exposed to the neutron beam. An incident beam ( $5 \times 5$  mm) of 0.7 to 3.5 Å bandwidth, allowing 0.5–2.5 Å d-space in the diffracted pattern of the  $\pm 90^\circ$  2 $\theta$  detector banks, was selected using the double-disk choppers at 30 Hz speed. High-intensity mode was employed with  $\Delta d/d \sim 0.4\%$ . Powder neutron diffraction data were collected in a high-intensity mode for a duration of 0.5 h and processed using VDRIVE software. Full pattern Rietveld refinement was performed using GSAS software, with EXPGUI interface.

### 2.1.9. Titration-gas Chromatography Analysis

The TGC experiments are performed using a Shimadzu GC-2010 Plus Tracera equipped with a barrier ionization discharge (BID) detector. The Split temperature was kept at 200 °C with a split ratio of 2.5 (split vent flow: 20.58 ml min $^{-1}$ , column gas flow: 8.22 ml min $^{-1}$ , purge flow: 0.5 ml min $^{-1}$ ). Column temperature (RT-MSieve 5A, 0.53 mm) was kept at 40 °C, and the BID detector was held at 235°C. Helium (99.9999%) was used as the carrier gas, and the BID detector gas flow rate was 50 ml min $^{-1}$ . The electrode sample was put in a septum-sealed glass vial, and after injecting the 0.5 mL H $_2$ SO $_4$  solution, the sample gases were injected into the machine via a 50  $\mu$ L Gastight Hamilton syringe. The detailed quantification of lithium loss is described in Figure S22, Supporting Information.

## 2.2. Computational Methods

### 2.2.1. Standard MD Simulations

Classical, fixed-charge Molecular Dynamics (MD) simulations were performed in LAMMPS using the General Amber force-field for solvents and Li $^+$  with the anion described with OPLS-AA potentials and charges of Kumar et al.<sup>[38]</sup> Liquid simulation boxes were constructed from random distributions of the molecules, with 38 LiPF $_6$ , 171 EC, and 257 EMC molecules for Gen 2 and 40 LiPF $_6$ , 55 FEC, and 374 MP molecules for M9F1. In all cases the charges of the Li $^+$  and PF $_6^-$  molecules were scaled to the high-frequency dielectric properties of the solvents present in the system according to the method employed by Park et al.<sup>[39]</sup> which is 0.73 for M9F1 and 0.72 for Gen 2. Periodic boundary conditions were applied in all directions.

For each system, an initial energy minimization at 0 K (energy and force tolerances of 10 $^{-4}$ ) was performed to obtain the ground-state structure. After this, the system was slowly heated from 0 K to room temperature at constant volume over 0.01 ns using a Langevin thermostat, with a damping



parameter of 100 ps. The system was then subjected to 5 cycles of quench-annealing dynamics in order to eliminate the persistence of any meta-stable states, where the temperature was slowly cycled between 298 K and 894 K with a ramp period 0.025 ns followed by 0.1 ns of dynamics at either temperature extreme. All 5 anneal cycles thus take 1.25 ns total. After annealing, the system was equilibrated in the constant temperature (Table S1, Supporting Information), constant pressure (1 bar) (NpT ensemble) for 1.5 ns. In the system isotropically using the Andersen barostat (pressure relaxation constant of 1 ps) stressed was resolved. Finally, 10 ns of constant volume, and constant temperature (NVT) production dynamics was performed. Visualized simulation boxes were generated in VMD.

### 2.2.2. MD Metadynamics Simulations

MD simulation boxes after equilibration (Standard MD section) were used as initial configuration for the free energy sampling with the metadynamics protocol. This protocol was applied in a 2D fashion with respect to Li<sup>+</sup>/EMC or Li<sup>+</sup>/MP distance (defined by center-of-mass) and coordination number based on the following definition of CN:

$$\sum_{i=1}^N \frac{1 - \left(\frac{r_i}{r_0}\right)^p}{1 - \left(\frac{r_i}{r_0}\right)^q} \quad (4)$$

where  $p = 6$  and  $q = 12$ .  $r_i$  is the distance between Li<sup>+</sup> and the  $i$ -th coordinating atom. In this case, only the solvent carbonyl oxygen was considered as a coordinating species, consistent with observations from the RDF analysis.  $r_0$  is the cut-off radius that defines atoms as inside or outside of the first solvation sphere, where  $i$  runs over the range that includes all possible coordinating atoms. The applied cut-off radius was 3.25 Angstroms. The simulations were carried out using the Colvars module in LAMMPS. In Table S1, Supporting Information, the parameters of the metadynamics free energy sampling for various simulations: height of the Gaussian hills (kcal/mol), frequency of hill creation (steps), the width of hills in Å for electrode distance or unitless for CN, and simulation time in ns was summarised. The free energy profiles shown in this work were averaged over the last 100 ns using Python and set to the same maximum free energy value for comparison. 2D profiles were generated in gnuplot.

### 2.2.3. Quantum Chemistry Calculations

Quantum chemistry simulations were performed using the Q-Chem 5.1 quantum chemistry package. Ionization potential and electron affinity simulations (Figure S2, Supporting Information) involved a geometry optimization step at the M06-HF//6-31+G(d,p) level of theory followed by single point energy measurement in neutral, oxidized, and reduced states at the M06-HF//6-311++G\*\* level of theory. Solvent removal simulations (Figure S8, Supporting Information) involved a

geometry optimization step at the B3LYP//6-31+G(d,p) level of theory where binding energy was calculated as follows:

$$\Delta E = \left( E_{\text{Li}^+(\text{MP})_3} + E_{\text{MP}} \right) - E_{\text{Li}^+(\text{MP})_4} \quad (5)$$

or

$$\Delta E = \left( E_{\text{Li}^+(\text{EMC})_2(\text{EC})} + E_{\text{EMC}} \right) - E_{\text{Li}^+(\text{EMC})_3(\text{EC})}$$

## 3. Result and Discussion

### 3.1. Electrolyte Impact in Extreme Fast Charging LIBs

Carboxylate ester systems have been shown to improve the energy retention of cells at reduced temperature due to their beneficial physicochemical properties.<sup>[27,28,36,40]</sup> We have applied similar MP/FEC electrolytes for improving low-temperature performance retention, establishing a clear correlation between systems designed for low-temperature and those designed for high-rate is a useful endeavor.<sup>[41,42]</sup> Additionally, the well-understood, inherently kinetic temperature scaling relationships of this system makes it an ideal platform to investigate improvement strategies for the failure modes associated with long-term XFC cycling. However, the long-term cycling performance of cells utilizing such solvents requires consideration of their electrochemical stability and kinetic benefits. To evaluate the impact of ester selection, the long-term stability of 250 mAh NMC 622 || graphite pouches (Figure 1a) was assessed by comparing methyl acetate (MA), MP, and methyl butyrate (MB) with a 10% FEC additive. This FEC additive has been previously demonstrated as the minimum amount required for stable graphite cycling.<sup>[27,41]</sup> As shown in Figure S1, Supporting Information, MA/FEC and MB/FEC were found to be less desirable for XFC applications, resulting in capacity retentions of 55.3% and 80.3% after 500 cycles. Instead, we find that the M9F1 system exhibited optimal characteristics, retaining 88.2% capacity under the same conditions. We hypothesize that this optimum is a product of a balance between electrochemical stability and viscosity, where MP shows an improved reductivity compared to MA (Figure S2, Supporting Information), at a reduced molecular size relative to MB. The MP/FEC ratio of 9:1 was also found to be optimal in terms of discharge capacity retention during a 4 C charge (Figure S3, Supporting Information).

To understand the performance advantages of M9F1 over a state-of-the-art carbonate system (Gen 2), pouch cells employing each electrolyte were constructed and subjected to a 4 C constant charging protocol and a C/3 discharge. Under such conditions, the cell employing Gen 2 exhibited 73.4% of its C/10 capacity in addition to a substantial and progressive increase in voltage polarization and a rapid decline in capacity to 54.1% after 500 cycles (Figure 1b, c). In contrast, the M9F1 cell was found to retain 82.5% of C/10 energy and retains 88.2% and 77.9% of this capacity after 500 and 1000 cycles with minimal loss in output voltage over the cycling duration (Figure 1b, d). To ensure that M9F1 is also compatible with typical constant current-constant voltage (CC-CV) charging procedures, this protocol was also applied with a total charging time cutoff of 15 (4 C), 10 (6 C), and 6 (10 C) min. Under such conditions,

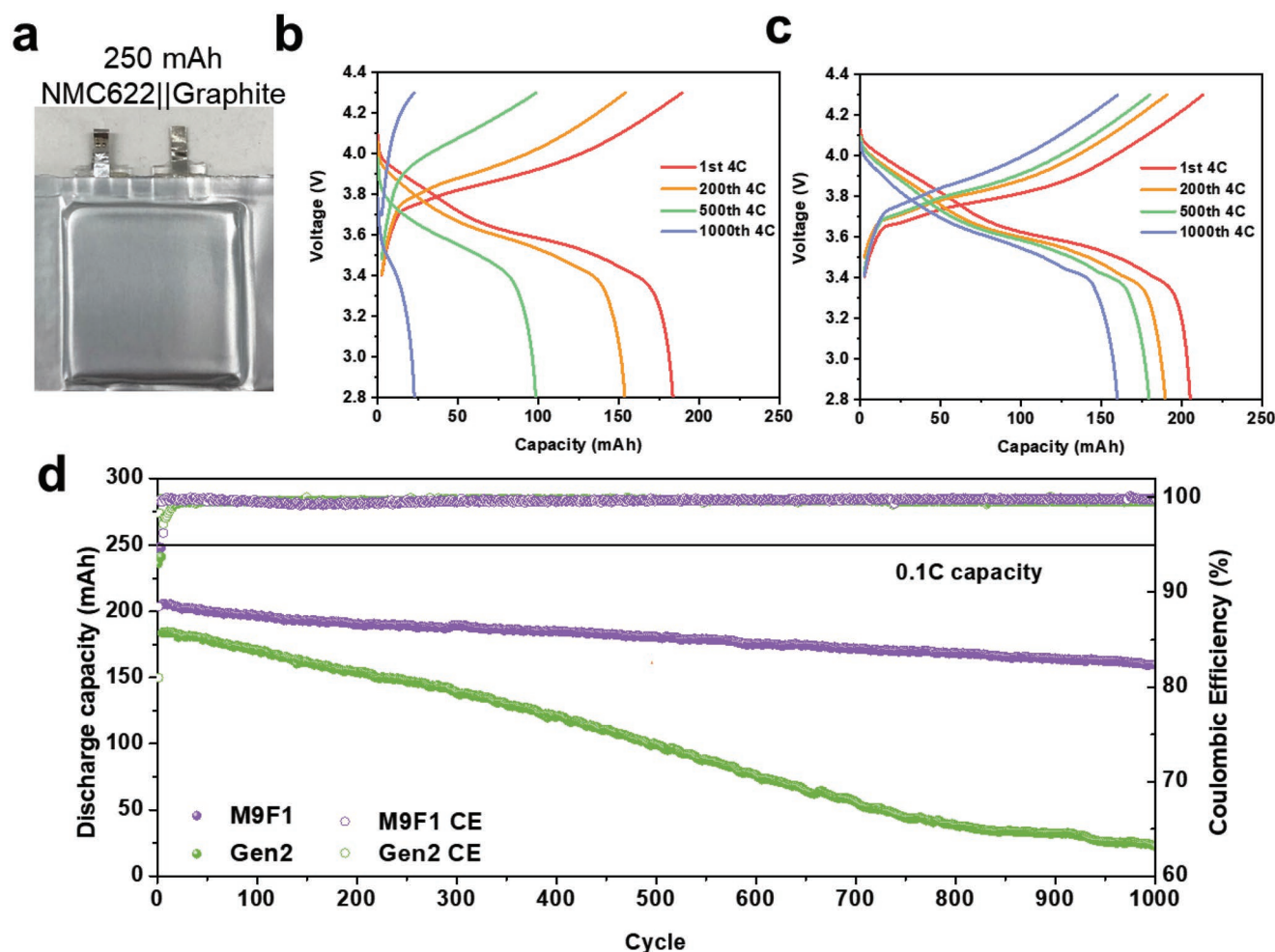


**Figure 1.** Dependence of XFC performance on electrolyte in pouch cells. a) Photograph of 250 mAh NMC 622||graphite pouch cells applied in this work. b) Cycling performance of pouch cells in electrolytes of interest. Voltage profiles over 4 C constant current cycling duration in c) Gen 2, and d) M9F1 electrolytes.

M9F1 cells achieved 86.95%, 85.53%, and 84.43% discharge capacity of its C/10 capacity for only 15 min, 10 min, and 6 min charging, respectively (Figure S4, Supporting Information). In addition, those M9F1 cells obtained capacity retention of 85.9% and 71.8% after 500 cycles of 4C and 6C fast charging, respectively (Figure S5, Supporting Information).<sup>[2]</sup> To our knowledge, such cycling stabilities under 6C fast-charging conditions have only been produced by a specialized carbonate-phosphate-nitrile blend on the order of 50 repeated cycles.<sup>[31]</sup> Additionally, the improved XFC performance of M9F1 does not come at the expense of stability at typical rates, exhibiting stable long-term cycling at C/3 (Figure S6, Supporting Information). Though such an improvement in XFC performance as a result of electrolyte design is valuable, understanding the physiochemical properties required for said improvement is vital for future progress.

To provide a basis for the improvement in XFC performance and the following characterization of failure mode mitigation, we apply a series of experimental and computational characterization techniques to the electrolytes of interest. As shown in Figure 2a, the M9F1 system demonstrates an improved ionic

conductivity of  $12.1 \text{ mS cm}^{-1}$  at room temperature compared to  $8.25 \text{ mS cm}^{-1}$  and  $6.95 \text{ mS cm}^{-1}$  for Gen2 and 1 M LiPF<sub>6</sub> in EC/diethyl carbonate (DEC) (1:1), (commonly referred to as LP40), respectively. Moreover, we find that M9F1 also exhibits enhanced retention of this conductivity at reduced temperatures, retaining 7.66 and 2.48 at  $-20$  and  $-60$  °C, respectively. The improved ionic conductivity of M9F1 does not come at the expense of Li<sup>+</sup> transport selectivity, where the  $t_{\text{Li}^+}$  of M9F1 was determined to be 0.46, compared to 0.35 and 0.34 in Gen 2 and LP40, respectively (Figure 2b). A similar simultaneous increase in ionic conductivity and  $t_{\text{Li}^+}$  was observed via the implementation of LiFSI, and is a rare but sought after electrolyte characteristic.<sup>[29]</sup> To further investigate the wide operating temperature window of MP/FEC electrolyte system, thermogravimetric analysis (TGA) and differential scanning calorimetry (DSC) are conducted among Gen 2, M9F1, and M7F3 (Figure S7, Supporting Information). Even though the M9F1 behaves an obvious volatile property compared with Gen 2 due to its ester-based solvent, the thermal stability has been significantly improved by blending with high-proportioned carbonate (FEC). Even under 45 °C cycling, M9F1 still shows a good capacity retention of

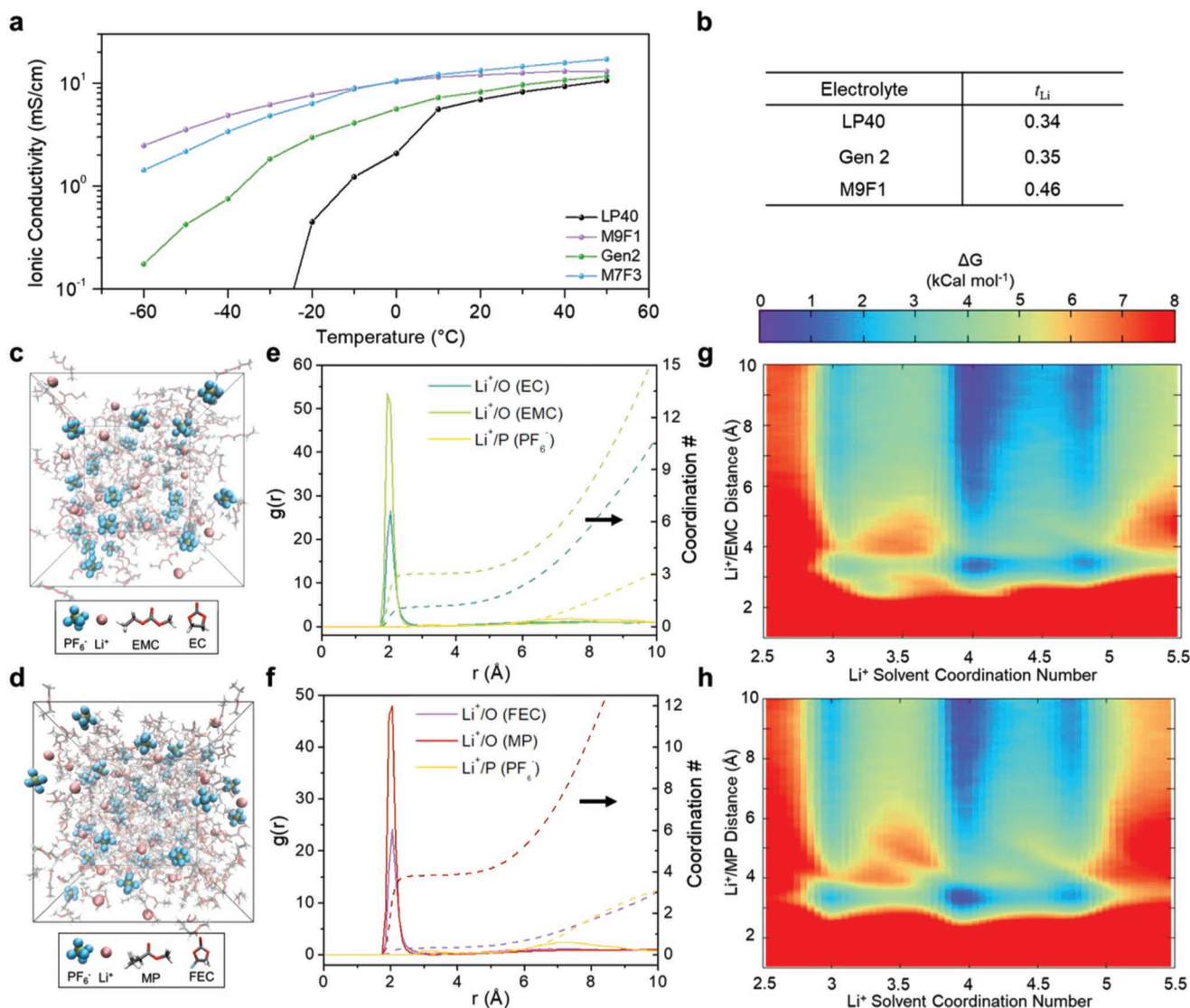


**Figure 2.** Experimental and simulated electrolyte properties. Measured a) ionic conductivity, and b)  $Li^+$  transference numbers of carbonate and carboxylate ester electrolyte of interest. Snapshots of MD simulations involving c) Gen 2, and d) M9F1 electrolytes. Calculated rdf and coordination numbers with respect to  $Li^+$  extracted from MD of e) Gen 2, and f) M9F1. 2-D free energy profiles with respect to  $Li^+$ /solvent coordination number and g)  $Li^+$ /EMC distance in Gen 2, h)  $Li^+$ /MP distance in M9F1.

90.7% after 100 cycles, which is comparable to Gen 2 electrolyte (Figure S8, Supporting Information) and with other ester systems.<sup>[30]</sup> Though such rapid, selective  $Li^+$  transport in the bulk electrolyte is known to be crucial for improved high-rate performance, factors impacting charge transfer at the interphase are also crucial to consider.

There is growing consensus that the  $Li^+$  desolvation portion of the charge-transfer process at the electrode is highly influential in electrochemical kinetics, and is fundamentally defined by the solvation structure of  $Li^+$  in the electrolyte.<sup>[11,33,36]</sup> To gain a more precise understanding of the underlying structure and behavior of these electrolytes at an atomic level, molecular dynamics (MD) simulations of the systems of interest were carried out in the manner outlined in materials and methods (Figure 2c, d). After equilibration, the radial distribution functions (RDFs) with respect to  $Li^+$  in M9F1 and Gen 2 were

computed and shown in Figure 2e,f. In terms of probability, it was found that EC and EMC were relatively comparable (Figure 2e), resulting in an average solvation structure of  $[Li(EMC)_{3.1}(EC)_{1.0}]^+$  (not equimolar due to overall molecular prevalence in the 7:3 mixture). On the other hand, we find that the most probable coordinating species in M9F1 is MP, resulting in an average structure of  $[Li(MP)_{3.8}(FEC)_{0.3}]^+$ . For both systems, it was found that there was negligible pairing between  $Li^+$  and  $PF_6^-$ , indicating that the improved transference number of M9F1 is not a result of ion-pairing. Rather, we hypothesize that the improved ionic conductivity and transference number in M9F1 is a direct result of the advantageous transport of MP itself, as shown by its improved diffusivity relative to EMC (Figure S9, Supporting Information). Though the movement of MP appears to be facile relative to EMC, whether or not such behavior results in facile desolvation is still relatively uncertain.



To answer this fundamental question, we apply a MD metadynamics free energy sampling technique which has been previously applied to understand the dynamic ion solvation behavior of  $Mg^{2+}$  and  $Li^+$  systems.<sup>[43–46]</sup> In doing so, we are able to explore multiple aspects of the electrolyte phase space, including states beyond what is thermally accessible through standard MD simulations. Though density functional theory (DFT) binding energy calculations are typically applied to understand this process, the above approach accounts for thermal motion and many body effects present in the electrolyte that would otherwise be ignored.<sup>[47–49]</sup> Specifically, we examine 2-dimensional free energy surfaces with respect to the coordination number of one  $Li^+$  and the distance between said  $Li^+$  and a coordinating solvent molecule (Table S1, Supporting Information). We only consider the removal of one coordinating solvent, which is generally considered to be the necessary step to induce electronic coupling between electrode and charge carrier, as the removal of all coordinating species typically produces activation barriers far too large to represent experimental measurements.<sup>[11,50]</sup> It is important to note that this analysis is carried out in the bulk electrolyte without the inclusion of an explicit electrode to obtain an indication of desolvation energetics, where the removal of one coordinating solvent molecule would otherwise be replaced by the electrode. While ideal, the inclusion of such an electrode would necessitate a 3-D free energy analysis, which is currently unfeasible.

When examining the 2D free energy profiles shown in Figures 2g,h, we consider a solvent removal pathway to be a reduction of coordination number (CN,  $x$ -axis) from the global minima of 4 to 3 with a simultaneous increase in the given EMC or MP distance. Note that this CN definition is strictly defined by cutoff distance (see Methods), in which the carbonyl oxygen of any solvent present in the system may contribute (MP, FEC, EMC, and EC). We take EMC/MP removal as the most probable removed species due to the increased dielectric of cyclic carbonates as well as the higher average CN of these species shown in the RDF analysis (Figure 2e,f). As shown in Figure S10, Supporting Information, this removal can proceed via 2 pathways, either by direct removal of the solvent (point A to C in Figure S10, Supporting Information), or by the detachment of the carbonyl oxygen via solvent rotation followed by removal (point A to B to C in Figure S10, Supporting Information). When examining the profiles for Gen 2 (Figure 2g) and M9F1 (Figure 2h) from this perspective, it is clear that the M9F1 system displays a well-defined pathway (point A to C) for direct removal within the energy range of  $\approx 5$  kcal mol<sup>-1</sup>, whereas the Gen 2 system exceeds 7 kcal mol<sup>-1</sup>. It is noteworthy that the removal of one such species is followed by the replacement of the coordination site by either a single-bonded oxygen or a  $PF_6^-$  (neither contributes to the defined CN), however, the initial removal contributes largely to the energy penalty. While the energetics of this replacement may diverge slightly in the investigated systems, we find that the formation of the lower CN = 3 state in quantum chemistry simulations is significantly more facile in M9F1, which further indicates that MP removal from  $Li^+$  in M9F1 faces a significantly lower barrier than EMC removal from  $Li^+$  in Gen 2 (Figure S11, Supporting Information). The facile desolvation

behavior of M9F1 is also supported by the significant reduction of charge transfer impedance shown in Figure S12, Supporting Information, and its substantially improved performance at  $-40$  °C over Gen 2, where desolvation is known to define performance (Figure S13, Supporting Information).<sup>[51,52]</sup> Despite the clear physiochemical advantages of M9F1, the effect of these properties on the LIB failure modes introduced by XFC conditions is necessary to fully understand the influence of electrolyte design on performance.

### 3.2. Identification and Mitigation of Active $Li^+$ Loss

To understand the origin of capacity loss in each cell, we conduct titration gas chromatography (TGC) analysis of graphite anodes in the discharged state after 1000 cycles in each electrolyte of interest. This technique allows for the differentiation between the capacity lost to metallic Li and  $Li^+$  in the SEI through quantification of  $H_2$  produced after the reaction of the ostensibly delithiated anode with a protic solvent (Figure 3a).<sup>[53,54]</sup> While TGC has been previously applied to quantify the amount of “dead” Li formed during Li metal cycling in various electrolytes, similar chromatography has been recently applied to graphite anodes cycled under fast-charge protocols, were reacted and unreacted in the SEI and the electrode, respectively can be differentiated.<sup>[55,56]</sup> We apply TGC here to differentiate between Li lost to SEI formation, and remaining reactive Li, which may exist as dead  $Li^0$ , or  $LiC_x$  in each electrolyte of interest. It is crucial to note that the latter may be active or inactive, where active  $Li^+$  would be trapped within the anode as a result of cathode degradation or increased anode polarization. When applied to the discharged graphite anodes harvested after 1000 XFC cycles in Gen 2 and M9F1, we find that 23% of capacity loss after 1000 cycles in Gen 2 can be attributed to SEI growth, compared to only 3% in M9F1. This 20% difference between cells implies that SEI growth during cycling is continuous, and is likely a result of the growth of Li metal and/or the exfoliation of said graphite during XFC charge.<sup>[2,9]</sup> This excessive capacity loss in Gen 2 clearly implies the formation of excessive reactive sites for decomposition during cycling, where the cell employing M9F1 produced only 0.17 mL of gas after 100 cycles compared to 0.66 mL in Gen 2 (Figure S14, Supporting Information). Moreover, 63% of the capacity loss after 1000 cycles in Gen 2 can be attributed to irreversible  $LiC_x$  or  $Li^0$ , compared to only 19% in M9F1. The morphology evolution of cathodes reveals no significant changes after 1000 cycles of fast cycling even at such a high amount of Li loss from NCM particles (Figure S15, Supporting Information). Through monitoring the lattice parameters evolution from the cathode side via neutron diffraction mapping, we also find that this  $Li^+$  loss is relatively uniform throughout the pouch cell (Figure S16, Supporting Information). Such degradation is in agreement with the work from Liu et al., and is likely a result of loss in  $Li^+$  inventory due to the aforementioned effects.<sup>[9]</sup> However, the origin of this excessive SEI growth and irreversible Li requires further characterization.

To probe the existence of Li metal during XFC charge in Gen 2, we first compare the differential capacity/voltage ( $dQ/dV$ ) profiles of cells employing the electrolytes of interest during



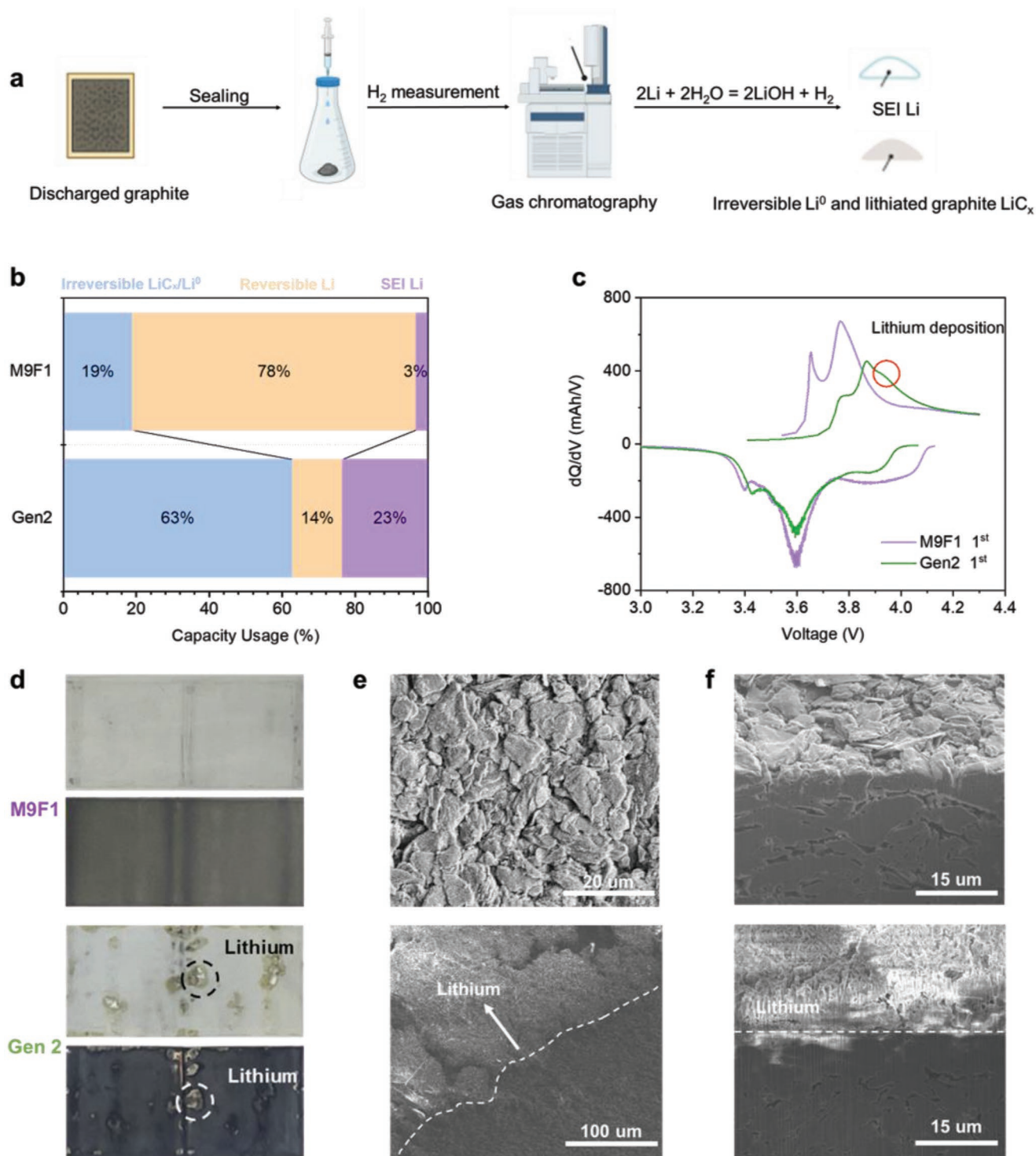


**Figure 3.** Quantification of capacity loss under XFC conditions and direct evidence of Li plating. a) Titration gas chromatography, and b) Quantification of Li loss in cells after 1000 XFC cycles. c) dQ/dV profile of 1<sup>st</sup> cycle of XFC cells in Gen 2 and M9F1 consisting of a 4 C charge and C/3 discharge. d) Optical photograph of separators and anodes harvested from pouch cells after 1000 cycles in Gen 2 and M9F1. SEM images of graphite anodes after cycling in Gen 2 and M9F1; e) top-view, and f) cross-section SEM image after FIB milling.

their first cycle. As shown in Figure 3c, the 4 C charging profile of Gen 2 exhibits substantially increased polarization compared with M9F1, with a third peak present at high voltage, implying

the formation of another phase during charge. As this peak is clearly not visible in either the M9F1 XFC profile, or in either electrolyte at 0.1 C (Figure S17, Supporting Information), it is

highly probable that this peak represents Li plating as a result of excessive polarization.<sup>[2,10,11]</sup> When disassembled, metallic Li was also observed on both the anode surface and the separator of cells employing Gen 2, further confirming this conclusion (Figure 3d). In comparison, there was no visible Li<sup>0</sup> found on either the separator or anode of the cell employing M9F1, even when fully un-wound (Figure S18, Supporting Information). When examined under SEM, plated Li<sup>0</sup> was also clearly observed on the surface of the graphite anode cycled in Gen 2, which was also found to be covered in a considerable SEI layer, given the poor conductivity of the material during imaging (Figure 3e,f). As a comparison, no metallic Li was observed on top or between the particles of the M9F1-cycled anode, which exhibited a morphology comparable to the pristine electrode (Figure 3e,f, Figure S19, Supporting Information). It is also noteworthy that no plated Li was observed in the other carboxylate ester electrolytes of interest, whereas the LP40 system displayed Li growth far beyond that of Gen 2. Though the improved transport and charge-transfer behavior of the M9F1 system are likely highly influential in the mitigation of Li plating during XFC cycling, further characterization of the formed SEI is also necessary to determine compositional or thickness variance that may contribute to the disparate kinetics.

### 3.3. Rate-Driven SEI Growth, Cointercalation and Interstitial Decomposition

To determine any variations in SEI composition between cells employing Gen 2 and M9F1, we first examine its thickness via cryogenic transmission electron microscopy (cryo-TEM). This analysis revealed that the interphase formed after 1000 cycles in Gen 2 was ≈20–30 nm thick, compared to M9F1, which was ≈10–15 nm (Figure 4a,b). Further, X-ray photoelectron spectroscopy (XPS) measurements also reveal significant compositional differences between the two systems. The compositional analysis of surface spectra from Figures S20 and S21, Supporting Information, are shown in

Figure 4c-e. We find that in addition to the thickness differences, the SEI formed in M9F1 demonstrated a substantially larger LiF/Li<sub>x</sub>PF<sub>y</sub> ratio, indicative of more effective passivation and aligned with Cryo-TEM results. Further, a substantially lower ratio of ROCO<sub>2</sub>Li/Li<sub>2</sub>CO<sub>3</sub> species are found in M9F1, which are generally believed to be suboptimal for Li<sup>+</sup> migration through the SEI.<sup>[5,56]</sup> Generally, we also find that the SEI formed in M9F1 contains more fluorine, and maintains a more homogenous composition than that formed in Gen 2 and LP 40 (Figure S22, Supporting Information). However, we do notice a

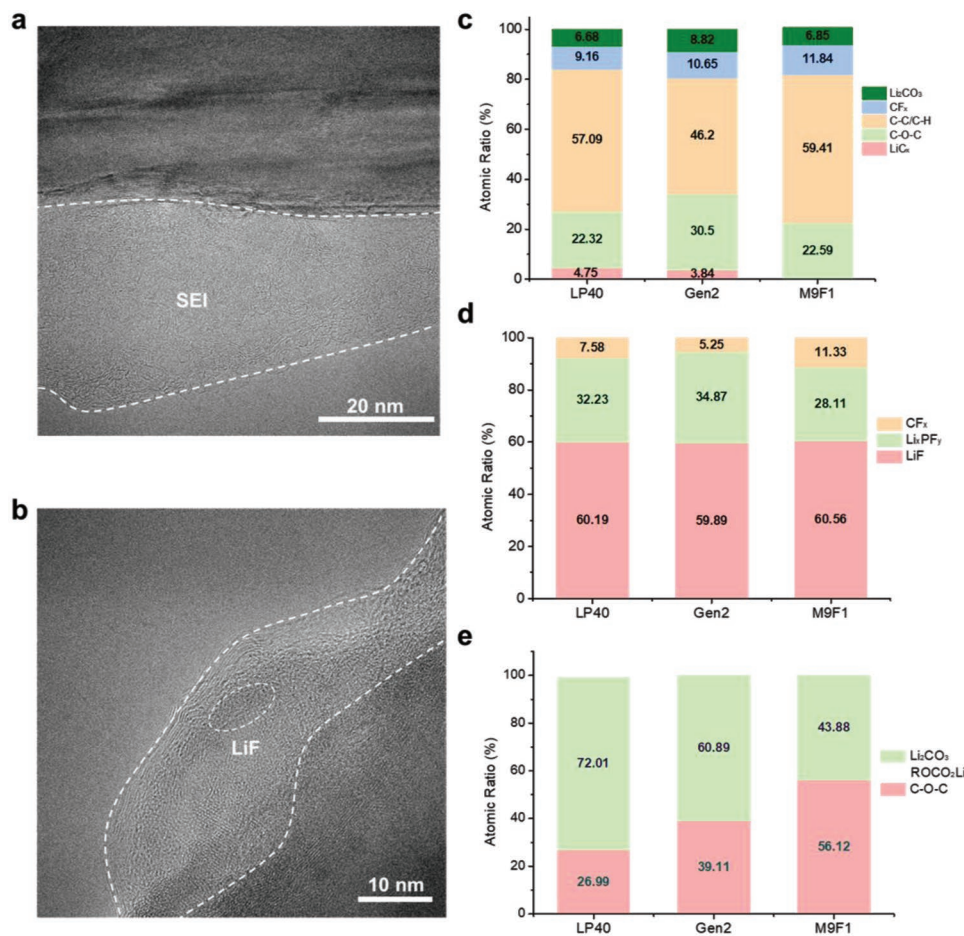


**Figure 4.** SEI characterization of anodes cycled in electrolytes of interest. Cryo-TEM images of the graphite surface after 1000 cycles in a) Gen 2, and b) M9F1. XPS compositional analysis from c) C 1s, d) F 1s, and e) O 1s spectra of anodes cycled in electrolytes of interest.



significant discrepancy in the XPS data, where  $\text{LiC}_x$  is observed in the Gen 2 surface spectra, which would not be expected given the larger thickness of its SEI relative to M9F1, and should in principle exceed the XPS sampling depth of  $\approx 10$  nm. A closer examination of this finding reveals another source of capacity loss for the Gen 2 system which further highlights the importance of rapid charge transfer for XFC applications.

Throughout the history of LIB development, the mitigation of  $\text{Li}^+$ /solvent co-intercalation between graphene sheets has been a critical step toward the stabilization of long-term

anode cycling.<sup>[57,58]</sup> While the well-known transition from propylene carbonate (PC) to EC has effectively solved this issue under standard operating conditions due to the formation of a solvent-shedding SEI, the fact remains that the activation energy for  $\text{Li}^+$ /solvent co-intercalation has been measured to be roughly half that of intercalation including de-solvation.<sup>[59]</sup> For this reason, it has been proposed that high kinetic stress such as XFC charging may result in the co-intercalation of  $\text{Li}^+$ /solvent complexes, which would then further exfoliate the graphite layers, leading to poor cycling stability.<sup>[2,10,11]</sup> As the activation

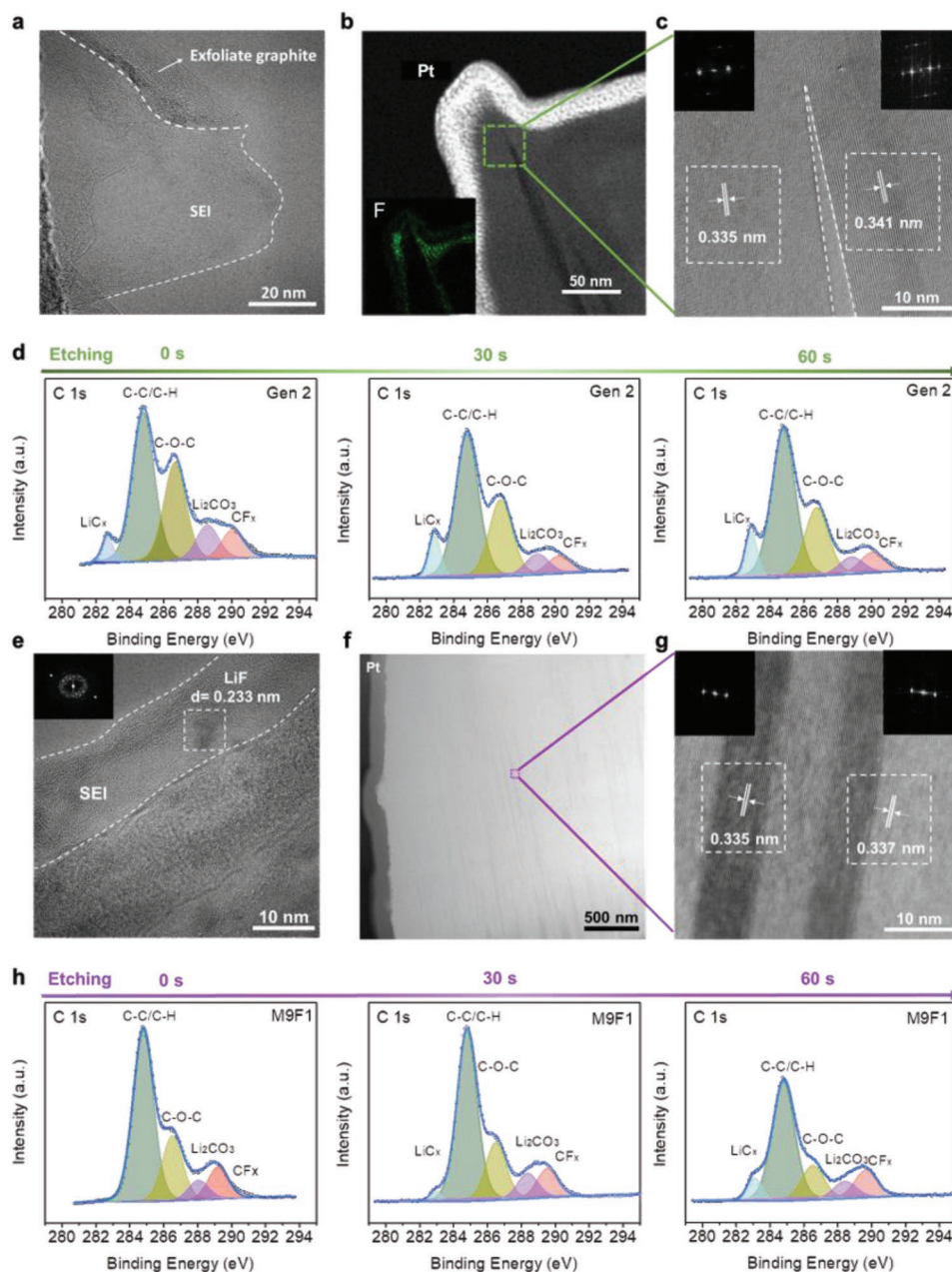


**Figure 5.** Evidence of exfoliation and interstitial SEI formation in graphite cycled under XFC conditions. Cryo-TEM images of graphite after 1000 XFC cycles in Gen 2. a) Cryo-TEM image of exfoliated graphite with interstitial SEI formation between graphene sheets. b,c) Cryo-STEM images of the cycled graphite FIB lamella with fluorine EDS inset. d) XPS C1s spectra of graphite cycled in Gen 2 at various stages of etching. Cryo-TEM images of graphite after 1000 XFC cycles in M9F1. e) Cryo-TEM image of graphite without the presence of exfoliation. f,g) Cryo-STEM images of the cycled graphite FIB lamella. h) XPS C1s spectra of graphite cycled in M9F1 at various stages of etching.



energy of desolvation relative to co-intercalation at the interphase directly governs this phenomenon, we conclude that the improved de-solvation mechanics of M9F1 gave rise to an intrinsic advantage in this regard.

By conducting cryo-TEM investigations of the graphite anode cycled in Gen 2, multiple incidents of such exfoliation events were observed (Figure 5a). Further, it is clear that the co-intercalation of such complexes resulted in substantial SEI growth between graphene sheet, effectively increasing the active area for electrolyte decomposition to a degree that we believe to be significant in the aforementioned SEI loss discrepancy. To further study the SEI penetration into the bulk of the graphite particles, focused ion beam (FIB) lamella of the cycled graphite powders was prepared and studied using cryogenic aberration-corrected electron microscope (Cryo-AC-STEM). After cycling in Gen 2, the graphite showed nanometer-thick cracks penetrating into the bulk particles (Figure 5b). Energy-dispersive X-ray spectroscopy (EDS) mapping of the same region showed enrichment of O, F, and P signals within the crack, which further showcased the co-intercalation of the solvent and anions followed by interstitial decomposition between the graphene layers (Figure S23, Supporting Information). Through further zooming in at the origin of the crack in Figure 5e, the bright field (BF) image also reveals that there is a significant *d*-spacing difference between graphite on the right side ( $\approx 0.341$  nm) and the left side ( $\approx 0.335$  nm), which implies that graphite within exfoliated regions may struggle to be fully delithiated. Evidence of such exfoliation was also observed in both Raman spectroscopy and X-ray diffraction of the cycled anodes, which reveals a substantially higher D/G ratio and *d*-spacing for the anode cycled in Gen 2 (Figure S24, Supporting Information). We propose that the exfoliation of such lithiated graphite domains leads to the observation of  $\text{LiC}_x$  in the XPS spectra of the Gen 2 system at significantly more shallow sampling depths (Figure 5d,e).

In comparison, no signs of significant graphite exfoliation or interstitial SEI growth was observed in the graphite cycled in M9F1, which demonstrated a uniform SEI consistent with the previously presented images (Figure 5f and 4b). Furthermore, FIB lamella of the cycled graphite in M9F1 indicated no signs of cracking or cointercalation inside the bulk of the particles, as shown in the cross-section low-magnification high-angle annular dark field (HAADF) image in Figure 5g. We also find that the *d*-spacing of graphite layers within the bulk are substantially more homogenous than that of Gen 2, which were observed to be between 0.337 and 0.335 nm (Figure 5h). Additionally, XPS spectroscopy at various etching depths reveals an intuitive trend, where the outer SEI regions do not show detectable  $\text{LiC}_x$  species, the signal for which slowly increases as the bulk of the particle is reached during etching (Figure 5i). In addition to the mitigation of Li plating and increased cell polarization during cycling, the optimized physiochemical properties of M9F1 effectively resolve rate-induced co-intercalation, exfoliation, and interstitial SEI formation.

## 4. Conclusion

In this work, we make significant progress towards achieving commercially viable LIBs charged at 15 min or less through the

comprehensive design of the battery electrolyte. Specifically, employing M9F1, a carboxylate-ester-based system results in a substantial improvement in XFC performance, retaining 82.5% of C/10 energy when charged at 4 C compared to only 73.4% in identical cells employing Gen 2. Crucially, cells employing M9F1 also demonstrated 88.2% capacity retention after 500 cycles, compared to only 54.1% in Gen 2. We find that this rapid capacity loss in Gen 2 is a result of a combination of Li plating, poor SEI characteristics, the cointercalation of  $\text{Li}^+$  /solvent complexes, and excessive gassing, resulting in graphite exfoliation and interstitial SEI formation. On the other hand, the rapid, selective  $\text{Li}^+$  transport, and facile  $\text{Li}^+$  desolvation provided by the M9F1 system was found to successfully mitigate all of the aforementioned failure modes, and is responsible for the state-of-the-art performance. This work highlights the various electrolyte characteristics responsible for improved fast-charging performance while demonstrating the origin of benchmark-exceeding electrochemical behavior.

## Supporting Information

Supporting Information is available from the Wiley Online Library or from the author.

## Acknowledgements

This work was supported by UC San Diego. Part of the work used the UCSD-MTI Battery Fabrication Facility and the UCSD-Arbin Battery Testing Facility. Neutron diffraction work was carried out at the Spallation Neutron Source (SNS), which is the U.S. Department of Energy (DOE) user facility at the Oak Ridge National Laboratory, sponsored by the Scientific User Facilities Division, Office of Basic Energy Sciences. The authors thank Dr. Y. Chen and Dr. K. An at SNS for their support of neutron experiments. The authors acknowledge the support of the Center for Synthetic Control Across Length-scales for Advancing Rechargeables (SCALAR), an Energy Frontier Research Center funded by the United States Department of Energy, Office of Science, Basic Energy Sciences under Award No. DESC0019381, for the microscopy and interface characterization. TEM experiments were conducted using the facilities in the Irvine Materials Research Institute (IMRI), which is supported in part by the National Science Foundation through the UC Irvine Materials Research Science and Engineering Center (DMR-2011967).

## Conflict of Interest

A patent associated to this work is under filing through the UC San Diego Office of Innovation and Commercialization.

## Data Availability Statement

The data that support the findings of this study are available from the corresponding author upon reasonable request.

## Keywords

cointercalation, extreme fast-charging, interstitial SEI formation, solvent desolvation

Received: August 26, 2022  
Revised: November 14, 2022  
Published online:

- [1] S. Chu, Y. Cui, N. Liu, *Nat. Mater.* **2017**, *16*, 16.
- [2] S. Ahmed, I. Bloom, A. N. Jansen, T. Tanim, E. J. Dufek, A. Pesaran, A. Burnham, R. B. Carlson, F. Dias, K. Hardy, M. Keyser, C. Kreuzer, A. Markel, A. Meintz, C. Michelbacher, M. Mohanpurkar, P. A. Nelson, D. C. Robertson, D. Scofield, M. Shirk, T. Stephens, R. Vijayagopal, J. Zhang, *J. Power Sources* **2017**, *367*, 250.
- [3] K. Xu, *J. Electrochem. Soc.* **2007**, *154*, A162.
- [4] K. Xu, A. Cresce, U. Lee, *Langmuir* **2010**, *26*, 11538.
- [5] G. Zhu, C. Zhao, J. Huang, C. He, J. Zhang, S. Chen, L. Xu, H. Yuan, Q. Zhang, *Small* **2019**, *15*, 1805389.
- [6] B. Babu, P. Simon, A. Balducci, *Adv. Energy Mater.* **2020**, *10*, 2001128.
- [7] T. R. Tanim, P. J. Weddle, Z. Yang, A. M. Colclasure, H. Charalambous, D. P. Finegan, Y. Lu, M. Preefer, S. Kim, J. M. Allen, F. L. E. Usseglio-Viretta, P. R. Chinnam, I. Bloom, E. J. Dufek, K. Smith, G. Chen, K. M. Wiaderek, J. N. Weker, Y. Ren, *Adv. Energy Mater.* **2022**, 2202795.
- [8] X. Wu, Y. Bai, Z. Li, J. Liu, K. Zhao, Z. Du, *J. Energy Chem* **2021**, *56*, 121.
- [9] T. Liu, Z. Du, X. Wu, M. M. Rahman, D. Nordlund, K. Zhao, M. D. Schulz, F. Lin, D. L. Wood, I. Belharouak, *Chem. Commun.* **2020**, *56*, 6973.
- [10] Y. Liu, Y. Zhu, Y. Cui, *Nat. Energy* **2019**, *4*, 540.
- [11] W. Cai, Y. Yao, G. Zhu, C. Yan, L. Jiang, C. He, J. Huang, Q. Zhang, *Chem. Soc. Rev.* **2020**, *49*, 3806.
- [12] P. P. Paul, V. Thampy, C. Cao, H.-G. Steinrück, T. R. Tanim, A. R. Dunlop, E. J. Dufek, S. E. Trask, A. N. Jansen, M. F. Toney, J. N. Weker, *Energy Environ. Sci.* **2021**, *14*, 4979.
- [13] J. Billaud, F. Bouville, T. Magrini, C. Villevieille, A. R. Studart, *Nat. Energy* **2016**, *1*, 16097.
- [14] K.-H. Chen, M. J. Namkoong, V. Goel, C. Yang, S. Kazemiabnavi, S. M. Mortuza, E. Kazyak, J. Mazumder, K. Thornton, J. Sakamoto, N. P. Dasgupta, *J. Power Sources* **2020**, *471*, 228475.
- [15] N. Kim, S. Chae, J. Ma, M. Ko, J. Cho, *Nat. Commun.* **2017**, *8*, 812.
- [16] Q. Cheng, R. Yuge, K. Nakahara, N. Tamura, S. Miyamoto, *J. Power Sources* **2015**, *284*, 258.
- [17] K.-H. Chen, V. Goel, M. J. Namkoong, M. Wied, S. Müller, V. Wood, J. Sakamoto, K. Thornton, N. P. Dasgupta, *Adv. Energy Mater.* **2021**, *11*, 2003336.
- [18] J. Betz, G. Bieker, P. Meister, T. Placke, M. Winter, R. Schmich, *Adv. Energy Mater.* **2019**, *9*, 1803170.
- [19] J. Liu, Z. Bao, Y. Cui, E. J. Dufek, J. B. Goodenough, P. Khalifah, Q. Li, B. Y. Liaw, P. Liu, A. Manthiram, Y. M. Meng, V. R. Subramanian, M. F. Toney, V. V. Viswanathan, M. S. Whittingham, J. Xiao, W. Xu, J. Yang, X. Yang, J. Zhang, *Nat. Energy* **2019**, *4*, 180.
- [20] E. J. Dufek, D. P. Abraham, I. Bloom, B.-R. Chen, P. R. Chinnam, A. M. Colclasure, K. L. Gering, M. Keyser, S. Kim, W. Mai, D. C. Robertson, M.-T. F. Rodrigues, K. Smith, T. R. Tanim, F. L. E. Usseglio-Viretta, P. J. Weddle, *J. Power Sources* **2022**, *526*, 231129.
- [21] A. M. Colclasure, A. R. Dunlop, S. E. Trask, B. J. Polzin, A. N. Jansen, K. Smith, *J. Electrochem. Soc.* **2019**, *166*, A1412.
- [22] A. M. Colclasure, T. R. Tanim, A. N. Jansen, S. E. Trask, A. R. Dunlop, B. J. Polzin, I. Bloom, D. Robertson, L. Flores, M. Evans, E. J. Dufek, K. Smith, *Electrochim. Acta* **2020**, *337*, 135854.
- [23] P. R. Chinnam, A. M. Colclasure, B.-R. Chen, T. R. Tanim, E. J. Dufek, K. Smith, M. C. Evans, A. R. Dunlop, S. E. Trask, B. J. Polzin, A. N. Jansen, *ACS Appl. Energy Mater.* **2021**, *4*, 9133.
- [24] M. Li, C. Wang, Z. Chen, K. Xu, J. Lu, *Chem. Rev.* **2020**, *120*, 6783.
- [25] B. Liao, H. Li, M. Xu, L. Xing, Y. Liao, X. Ren, W. Fan, L. Yu, K. Xu, W. Li, *Adv. Energy Mater.* **2018**, *8*, 1800802.
- [26] E. R. Logan, J. R. Dahn, *Trends Green Chem.* **2020**, *2*, 354.
- [27] E. R. Logan, D. S. Hall, M. M. E. Cormier, T. Taskovic, M. Bauer, I. Hamam, H. Hebecker, L. Molino, J. R. Dahn, *J. Phys. Chem.* **2020**, *124*, 12269.
- [28] M. C. Smart, B. L. Lucht, S. Dalavi, F. C. Krause, B. V. Ratnakumar, *J. Electrochem. Soc.* **2012**, *159*, A739.
- [29] Z. Du, D. L. Wood, I. Belharouak, *Electrochem. Commun.* **2019**, *103*, 109.
- [30] G. Xu, S. Huang, Z. Cui, X. Du, X. Wang, D. Lu, X. Shangguan, J. Ma, P. Han, X. Zhou, G. Cui, *J. Power Sources* **2022**, *416*, 29.
- [31] N. Gao, S. Kim, P. Chinnam, E. J. Dufek, A. M. Colclasure, A. Jansen, S.-B. Son, I. Bloom, A. Dunlop, S. Trask, K. L. Gering, *Energy Storage Mater.* **2022**, *44*, 296.
- [32] X. Wu, T. Liu, Y. Bai, X. Feng, M. M. Rahman, C.-J. Sun, F. Lin, K. Zhao, Z. Du, *Electrochim. Acta* **2020**, *353*, 136453.
- [33] B. Wen, Z. Deng, P. Tsai, Z. W. Lebens-Higgins, L. F. J. Piper, S. P. Ong, Y. Chiang, *Nat. Energy* **2020**, *5*, 578.
- [34] B. Huang, K. H. Myint, Y. Wang, Y. Zhang, R. R. Rao, J. Sun, S. Mui, Y. Katayama, J. C. Garcia, D. Fraggedakis, J. C. Grossman, M. Z. Bazant, K. Xu, A. P. Willard, S. Yang, *J. Phys. Chem.* **2021**, *125*, 4397.
- [35] Z. Wang, Z. Sun, Y. Shi, F. Qi, X. Gao, H. Yang, H. Cheng, F. Li, *Adv. Energy Mater.* **2021**, *11*, 2100935.
- [36] H. Cheng, Q. Sun, L. Li, Y. Zou, Y. Wang, T. Cai, F. Zhao, G. Liu, Z. Ma, W. Wahyudi, Q. Li, J. Ming, *ACS Energy Lett.* **2022**, *7*, 490.
- [37] R. Petibon, J. Harlow, D. B. Le, J. R. Dahn, *Electrochim. Acta* **2015**, *154*, 227.
- [38] N. Kumar, J. M. Seminario, *J. Phys. Chem.* **2016**, *120*, 16322.
- [39] C. Park, M. Kanduč, R. Chudoba, A. Ronneburg, S. Risse, M. Ballauff, J. Dzubiella, *J. Power Sources* **2018**, *373*, 70.
- [40] S. Hou, X. Ji, K. Gaskell, P. Wang, L. Wang, J. Xu, R. Sun, O. Borodin, C. Wang, *Science* **2021**, *374*, 172.
- [41] J. Holoubek, Y. Yin, M. Li, M. Yu, Y. S. Meng, P. Liu, Z. Chen, *Angew. Chem., Int. Ed.* **2019**, *58*, 18892.
- [42] Y.-G. Cho, M. Li, J. Holoubek, W. Li, Y. Yin, Y. S. Meng, Z. Chen, *ACS Energy Lett.* **2021**, 2016.
- [43] A. Baskin, D. Prendergast, *J. Phys. Chem. Lett.* **2019**, *10*, 4920.
- [44] A. Baskin, D. Prendergast, *J. Phys. Chem. Lett.* **2020**, *11*, 9336.
- [45] A. Baskin, J. W. Lawson, D. Prendergast, *J. Phys. Chem. Lett.* **2021**, *12*, 4347.
- [46] J. Holoubek, A. Baskin, J. W. Lawson, H. Khemchandani, T. A. Pascal, P. Liu, Z. Chen, *J. Phys. Chem. Lett.* **2022**, *13*, 4426.
- [47] J. Holoubek, H. Liu, Z. Wu, Y. Yin, X. Xing, G. Cai, S. Yu, H. Zhou, T. A. Pascal, Z. Chen, P. Liu, *Nat. Energy* **2021**, *6*, 303.
- [48] M. Okoshi, Y. Yamada, A. Yamada, H. Nakai, *J. Electrochem. Soc.* **2013**, *160*, A2160.
- [49] X. Fan, X. Ji, L. Chen, J. Chen, T. Deng, F. Han, J. Yue, N. Piao, R. Wang, X. Zhou, X. Xiao, L. Chen, C. Wang, *Nat. Energy* **2019**, *4*, 882.
- [50] L. M. C. Pinto, E. Spohr, P. Quaino, E. Santos, W. Schmickler, *Angew. Chem., Int. Ed.* **2013**, *52*, 7883.
- [51] Q. Li, D. Lu, J. Zheng, S. Jiao, L. Luo, C. Wang, K. Xu, J. Zhang, W. Xu, *ACS Appl. Mater. Interfaces* **2017**, *9*, 42761.
- [52] S. S. Zhang, K. Xu, T. R. Jow, *J. Power Sources* **2003**, *115*, 137.
- [53] C. Fang, J. Li, M. Zhang, Y. Zhang, F. Yang, J. Z. Lee, M. Lee, J. Alvarado, M. A. Schroeder, Y. Yang, B. Lu, N. William, M. Ceja, L. Yang, M. Cai, J. Gu, K. Xu, X. Wang, Y. S. Meng, *Nature* **2019**, *572*, 511.
- [54] W. Bao, C. Fang, D. Cheng, Y. Zhang, B. Lu, D. H. S. Tan, R. Shimizu, B. Sreenarayanan, S. Bai, W. Li, M. Zhang, Y. S. Meng, *Cell Rep. Phys. Sci.* **2021**, *2*, 100597.
- [55] E. J. McShane, H. K. Bergstrom, P. J. Weddle, D. E. Brown, A. M. Colclasure, B. D. McCloskey, *ACS Energy Lett.* **2022**, *7*, 2734.
- [56] E. J. McShane, A. M. Colclasure, D. E. Brown, Z. M. Konz, K. Smith, B. D. McCloskey, *ACS Energy Lett.* **2020**, *5*, 2045.
- [57] M. Winter, B. Barnett, K. Xu, *Chem. Rev.* **2018**, *118*, 11433.
- [58] T. Liu, L. Lin, X. Bi, L. Tian, K. Yang, J. Liu, M. Li, Z. Chen, J. Lu, K. Amine, K. Xu, F. Pan, *Nat. Nanotech.* **2019**, *14*, 50.
- [59] T. Abe, H. Fukuda, Y. Iriyama, Z. Ogumi, *J. Electrochem. Soc.* **2004**, *151*, A1120.
- [60] L. Benitez, J. M. Seminario, *J. Electrochem. Soc.* **2017**, *164*, E3159.